PROCEEDINGS, 50th Workshop on Geothermal Reservoir Engineering
Stanford University, Stanford, California, February 10-12, 2025
SGP-TR-229

Next Generation Reservoir Modeling for Geothermal Energy and Lithium Recovery

Colleen Barton[1], William Pettitt[1], Tim Salter[1], Elena Meyer[1], Christopher Harper[1], Ehsaan Nasir[1], Amir Moradi[1], Richard Alt[1], Fatmir Likrama[1], Danny Sims[2], William Osborn[2]

[1]Baker Hughes, [2]Controlled Thermal Resources (US) Inc.

Colleen.Barton@BakerHughes.com

Keywords: Salton Sea Geothermal Field, Lithium, Reservoir Simulation, Discrete Fracture Networks

ABSTRACT

The geothermal resource potential of the Hell's Kitchen area of the Salton Sea Geothermal Field (SSGF) was evaluated through geological assessment, well modeling, and reservoir simulation to deliver a natural state matched and dynamic reservoir model for estimating geothermal power potential and lithium production. An 8km x 8.5km 3D geomodel centered around the Hell's Kitchen development area was constructed from ground level down to a base depth that equals a nominal 370°C isotherm. The temperature model distinguishes the high geothermal gradient thermal cap from the near isothermal reservoir that is clearly demonstrated in most wells. A review of geochemical properties for the resource defined the key inputs to flow simulation of lithium rich and lithium depleted brines. The main reservoir faults define linear trends likely to host enhanced permeability or upflow of fluid from the base of the reservoir. A Discrete Fracture Network (DFN) model was developed to provide the fracture and fault derived permeability to the dynamic flow model. The DFN model comprises large-scale faults that are described deterministically and smaller scale structures that are described stochastically. Stress-permeability coupling is dynamically computed during DFN model development. To model flow and transport on the regional scale over time, the properties of the network of discrete fractures were upscaled to the geomodel grid.

The static model was imported into a commercial reservoir modelling package for dynamic simulation. Modeled pressure distribution at the natural state condition matched measured pressure and salinity data and provided an excellent match to a large spatial distribution of well temperature data. Forecast scenarios, designed to evaluate optimal initial stage production, were simulated for a 30-year forecast of enthalpy and lithium production. Sensitivities to production forecasts were tested for permeability magnitude, well location, and permeability distribution. These sensitivities illuminate the additional data and analyses required to reduce uncertainty in reservoir model forecasting. Results across multiple stages of development, combined with the permeability scenario tests, highlight the importance of gaining greater insight and robust field analyses for the in situ permeability field. The highly robust fit of the model relative to observed data gives a high level of confidence that the integrated geological framework of porosity, fracture and fault permeability, and reservoir flow regimes are being reasonably described. The next-generation techniques used in the modeling process also yielded a model that fits industry experience of the SSGF.

1. INTRODUCTION

The Hell's Kitchen Geothermal LLC (HKG) project is situated within the SSGF, one of the world's most active geothermal regions (Figure 1). Known for its high temperature mineralized brine and complex subsurface characteristics, the field is a critical resource for renewable energy and lithium production, a mineral essential for energy storage technologies. The HKG project seeks to capitalize on the dual potential of geothermal energy and critical mineral production, specifically lithium, by employing innovative reservoir management strategies. The sediment-hosted prograde magmatic hydrothermal system presents both opportunities and challenges for sustainable resource development. Effective modeling is essential for understanding subsurface dynamics and guiding operational decisions. Past studies, such as Araya & O'Sullivan (2022), explored fluid pathways and fault dynamics within the SSGF. This work differs by integrating advanced methodologies, such as developing and incorporating a hydrostructural Discrete Fracture Network (DFN) (Dershowitz et al., 2004) and the integration of a halocline boundary (Williams, 1997) into the dynamic flow modelling to provide more accurate forecasts and operational insights for development of SSGF.

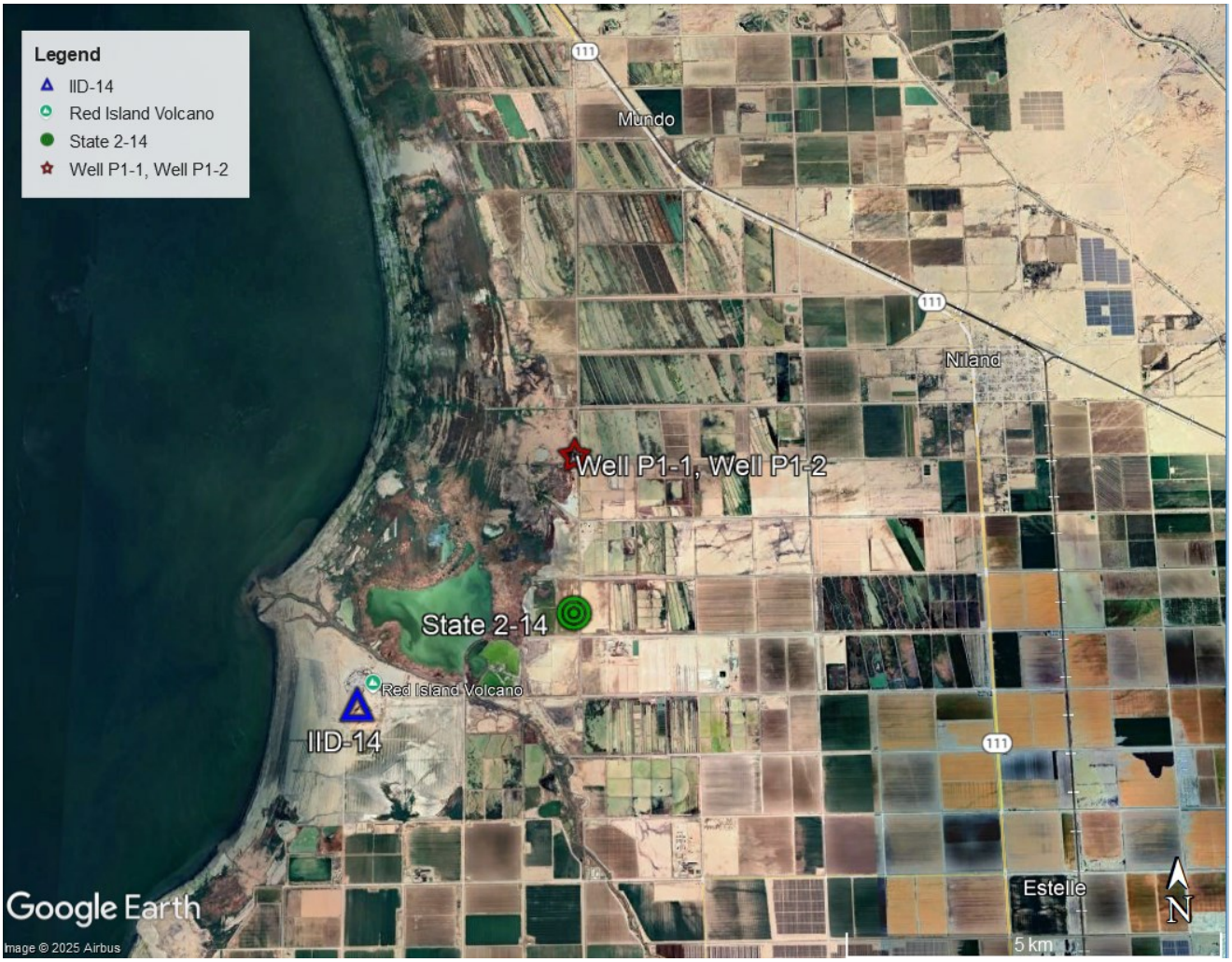

Figure 1: HKG project location within the Salton Sea Geothermal Field.

The primary purpose of this work was to evaluate a Stage1 development through natural state and dynamic numerical reservoir modeling for estimating geothermal power potential and lithium production and to evaluate production and injection strategies for long-term sustainable development for the HKG Project. The model considered the two existing HKG wells as producers with a third production well drilled between the two and four injection wells. Three Stage 1 scenarios were analyzed using three different potential injection field locations (Stage 1A, 1B, and 1C scenarios).

2. 3D GEOMODEL

An initial geological model, proprietary reports, presentations, and access to numerous published documents were provided by HKG. Building upon this framework, Baker Hughes constructed a geological model over an area of c. 8 x 8.5 km that captures the eastern half of the SSGF and is centered on the HKG Stage 1 development area. The grid is rotated 45° from north to align with regional-scale (NE-SW & NW-SE) intra-basin faults. The model was constructed from ground level down to the base of the dual porosity reservoir, which coincides with the clinopyroxene isograd, the 5.6 km/s velocity surface, and the 370°C isotherm (Sims and Neuhoff, 2018).

The stratigraphic zonation adopted is based upon metamorphic alteration (Figure 2, left). Alluvial sands and lacustrine shales that are stratigraphically above the 250-260°C isotherm have a chlorite-calcite metamorphic mineral assemblage at the base, grading up to dolomite-kaolinite altered rock, and then near-surface weakly altered sediments (Sims and Neuhoff, 2018). The chlorite-calcite mineral assemblage persists down to the biotite zone, located near the base of the dual porosity reservoir. Within the chlorite-calcite zone there is an onset of sodium feldspar (albite). This is the top of the feldspar zone, which coincides with the 250-260°C isotherm. The base of the feldspar zone is marked by the onset of biotite in the metamorphic mineral assemblage, and this is the stratigraphic top of the biotite zone. Below this, the onset of clinopyroxene marks the top of the clinopyroxene zone. The maximum depth of drilling in the SSGF penetrates the top several hundred feet of the clinopyroxene zone (Sims and Neuhoff, 2018).

The alteration model defines the thermal cap to comprise the 'unaltered' and 'chlorite' zones that are bound from ground level to the 175°C and the 175°C-260°C isotherms respectively. The thermal cap, as defined by Moore and Adams (1988), is a layer of weakly altered, vertically impermeable sediments. This stratigraphic interval above the top of the feldspar zone is a region of conductive heating with a steep geothermal gradient. The brine within this region is Low-Salinity (<40,000 ppm Na). The contact at the top of the feldspar zone marks a sharp transition from Low Salinity Brine above to High Salinity Brine (>40,000 ppm Na) below (Williams and McKibben, 1989; Sims and Neuhoff, 2018). This boundary is the Halocline (Sims and Neuhoff, 2018). Within the model, the halocline is a deterministic low permeability layer coincident with the 250-260°C isotherm, that minimizes vertical fluid movement between the High Salinity Brine and Low Salinity Brine zones (e.g., Williams, 1997).

Regional-scale faults included within the model are taken from the HKG database. The faults are identified on the basis of published geophysical studies, seismic activity and the alignment of surface geothermal features (Sims and Neuhoff, 2018; Sims, 2022). Some of the regional-scale faults are modelled to act as focal areas for high permeability within damage zones. Two regional fault intersections that are coincident with high thermal gradients are the locations of modelled upflow zones, and the model allows vertical heat and brine flow to ascend from below the clinopyroxene zone and into the dual porosity reservoir at these locations.

The geological model captures key elements of the dual porosity reservoir and allows numerical simulation of pressure, temperature and chemistry changes that occur when the system is perturbed by geothermal development wells. The final grid was coarsened both laterally and vertically by a factor of 2 to reduce the total number of grid cells to be simulated by 8x, while still retaining the underlying model heterogeneity. The model was used as the template in which to place a high definition discrete fracture network within the reservoir and remain faithful to the high-resolution grid.

2.1 Temperature Model

The 3D temperature model build followed previous such studies in combining different data sets. In order of importance these included individual well temperature vs. depth profiles (edited where considered necessary), previous isotherm maps for select depths/study areas; and inference from overall basin structure and faults controlling the SSGS.

The maximum reservoir temperature was taken to be as sampled by the IID-14 well at Red Island, which was drilled on the rhyolite volcano and passed into metamorphosed sediments downhole (GeothermEX, 1990, HKG database). The geothermal field is described as an elongate dome around this location (Figure 1). Where closely spaced well data are available, additional localized variability in temperature is also found, with lateral temperature variations of c.38°C /100m identified locally.

A key element of the temperature model (Figure 2, right) was to distinguish the halocline that separates a Low Salinity Brine region (with a high conductive geothermal gradient) from the High Salinity Brine reservoir that has a near isothermal gradient owing to a convective system. This break from conductive heating to convective heating thermal profiles is clearly demonstrated in most wells. The base of the dual porosity reservoir, defined by the onset of clinopyroxene in the stratigraphy, is less clearly defined in temperature logs but is likely associated with an increase in the geothermal gradient owing to reduced inter-granular permeability. By randomly sampling the temperature model at locations away from any input wells and then extracting the model temperature profile (as shown by the blue symbol in Figure 2, right) for a QC well [synthMI] at Mullet Island, (Figure 2, middle) it was possible to confirm the depth of the halocline/top of dual porosity reservoir was as expected, and that the change in geothermal gradient at this depth matched that expected conceptually for that part of the SSGF.

The variation in geothermal gradient was maintained through the 3D model volume using careful selection of interpolation parameters. This gave a conceptual dual porosity reservoir thickness of about 1830 m across the model, matching observations from nearby well State 2-14. The base of the model has been set at the base of the dual porosity reservoir and top of the fracture dominated reservoir (Sims and Neuhoff, 2018) at an expected temperature of approximately 370°C.

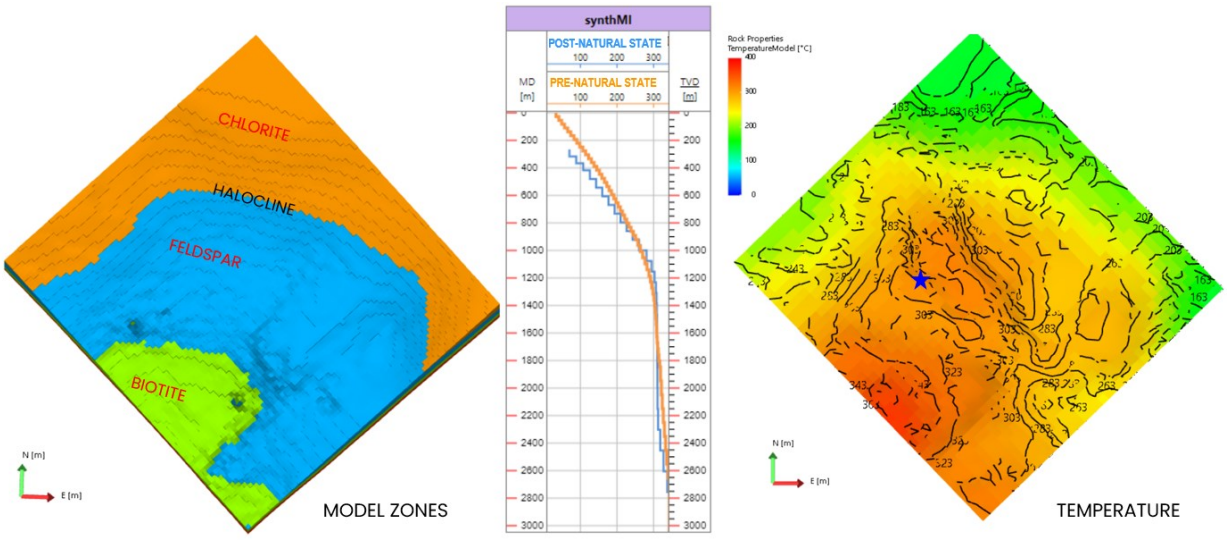

Figure2: Rock property slice at 1500m TVDSS (left), temperature profile extracted at indicated location (middle) and temperature slice at 1500m TVDSS (left)

2.2 Geochemistry

A review of geochemical properties for the HKG geothermal resource was used to define the key inputs to the simulation of the flow of lithium-rich High Salinity Brine native to the reservoir and post-process lithium-depleted brines that are injected back into the reservoir. Primarily, the focus of this part of the investigation was to define the lithium concentration distribution and brine densities, which are a function of temperature gradient and ionic composition variations.

The presence of a halocline at a temperature of approximately 260°C greatly affects the density gradient of the fluids within the formations being investigated. Brines above the halocline are significantly less saline and less dense than the brines immediately below the halocline (Williams and McKibben, 1989 and Dutcher et al., 1972) (Figure 3). Concentrations of lithium in the brine below the halocline would be approximately 220 ppm (Dobson et al., 2023). Under natural, or initial conditions, the resulting fluids do not mix due to their large difference in density. (Williams and McKibben, 1989).

Calculations of the density of the various dilutions of the fluids vs. temperature, across a range of salinities from 260 g/l (sub-halocline brine) to 26 g/l (above halocline brine) were performed to account for the non-linear behavior of sodium, potassium and calcium with temperature and chloride contents. Interpretation and calculation of density profiles in accordance with the measured temperature profiles from the P1-1 and P1-2 were then performed. Immediately above the halocline the brine densities are calculated to be as low as 0.795 SG, while immediately below the halocline the brine densities are calculated to be as high as 1.01 SG. The change in density provides a significant barrier to upwards convective flow of sub-halocline brine. The density of the reinjected fluid is anticipated to be 1.19 SG, as it is both higher salinity and lower temperature than the native brine below the halocline, which means, without agitation or horizontal stratification, this fluid should sink when reinjected into the reservoir.

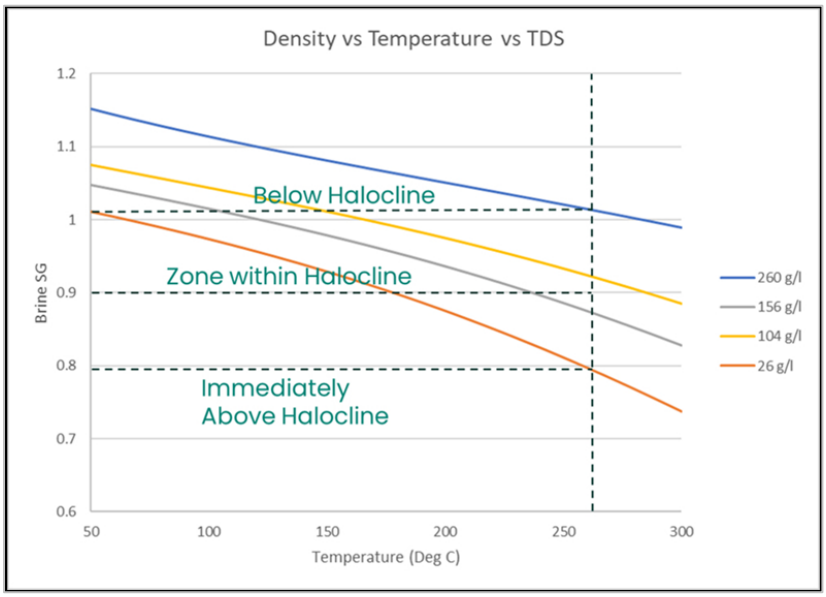

Figure 3: Density profiles for various salinity brines vs. temperature.

3. 1D TO 3D GEOMECHANICAL MODEL

1D geomechanical models were derived through analysis of log data acquired in wells P1-1 and P1-2 and the State 2-14 well to constrain the pore pressure, stress field, and rock strength properties as a function of depth. Bulk density logs were used to model the overburden stress. Measured pore pressure profiles indicate sub-hydrostatic absolute pressure consistent with regional water table data (Thompson et al., 2008).

Induced thermal tensile wall fractures observed in both wells provide an unequivocal NNE orientation of the maximum horizontal stress. These induced features imaged in the inclined interval of well P1-1 were used to invert for the horizontal stress magnitudes consistent with their azimuth and inclination at the wellbore wall. Using the observations of wellbore failure, measured pore pressure, and a thorough analysis of geomechanical events documented in daily drilling reports, 1D geomechanical modeling for all wells indicate a normal faulting stress state where the vertical stress, S_v, is the maximum principal stress, S1. These conclusions are consistent with conclusions of other studies that are based on well-scale and regional-scale studies (see Sims, 2022). The two horizontal stresses, S_{Hmax} and S_{hmin}, have an Effective Stress Ratio of 0.85 and 0.25 respectively.

A 3D geomechanical model was developed through the geomodel domain. Formation density from the HKG wells and the State 2-14 well, which is drilled to 3050 m, was mapped to the 3D volume. Overburden stress was then calculated through vertical integration of density from the surface to the base of the model and benchmarked against the 1D geomechanical models. The reservoir volume pore pressure model was constructed based on pore pressure profiles provided from wells P1-1 and P1-2, drilling mud weights and drilling mud losses. The geomechanical properties internal friction coefficient, dynamic Young's Modulus, dynamic Poisson's Ratio, minimum horizontal stress magnitude S_{hmin} and maximum horizontal stress magnitude S_{Hmax} were also property mapped through the 3D model. The maximum horizontal stress azimuth is assumed to be constant in the whole volume and equal to 10° east of north.

Pre-existing fracture sets optimally oriented to the current stress state are likely to be in failure and actively slipping in the present day. Because this action of shear failure along preexisting fractures principally drives the propagation of fluid through the subsurface, these fractures will be dilated and provide enhanced permeability conduits for fluid flow. Notwithstanding the shallow thermal anomaly and series of thermal features, including the Mullet Island volcano, located along the NW-SSE-striking Calipatria fault and thermal features located along the NNW-SSE-striking Wister fault, a 3D fault permeability analysis performed on the reservoir faults shows the major NNE-SSW trending faults have higher permeabilities than faults oriented in the NNW-SSE direction (Figure 4, right). In 1D, the pervasive north–south fractures that dip 60°-70° to the east and west are critically stressed and thereby enhance flow at a finer scale in the north-south direction (Figure 4, left). As discussed below, the three principal stresses magnitudes and orientations are critical input into building and characterizing the DFN.

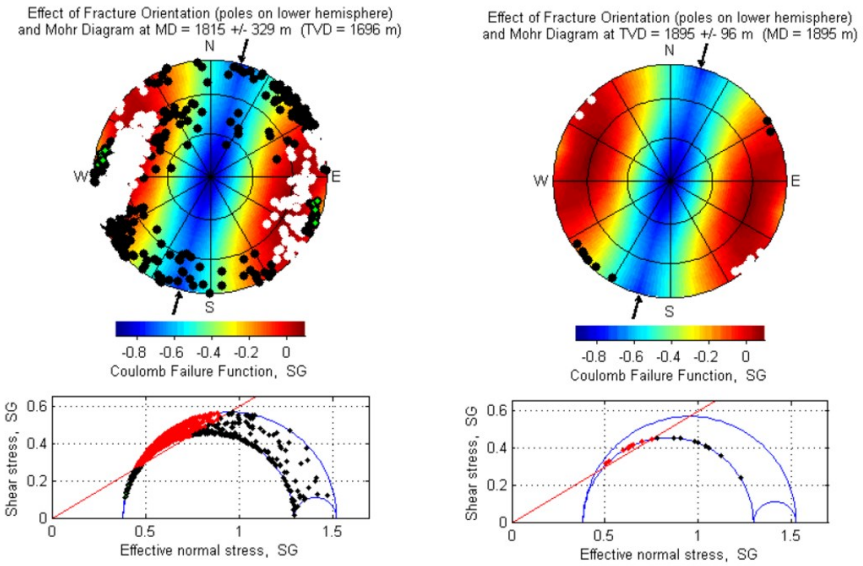

Figure 4. Geomechanical modeling to determine the likelihood of slip on planar features detected in electrical image data in well P1-2 (left) and model faults (right). Fractures and faults with a ratio of shear to effective normal stress greater than a coefficient of sliding friction of 0.6 are highlighted in white on the lower hemisphere projections and red on the Mohr Diagram.

4. PERMEABILITY NETWORK MODEL

A fracture network model was developed to provide the fracture and fault derived permeability to the dynamic flow model. The DFN model is composed of large-scale hydro-structures (faults) that can be described deterministically, and smaller scale structures that are described stochastically. The hydro-structural model is interpreted from the structural fault framework model Figure 5 top left). The stochastic distributions of fracture geometries of the base DFN model were consistent with fracture analyses in wells P1-1 and P1-2 (Figure 5, top right). The pervasive north striking sets observed in image log data are interpreted in this study to be associated with the current normal faulting extensional regime of the area and to be ubiquitous within the SSGF (Sims, 2023). A distance to faults fracture distribution was applied to the base fracture network model that assumes fault damage zones may develop a large number of fractures crosscutting the adjacent host rocks, where the length and density of fractures would decrease as a function of distance from the fault centerline (Ru Jia et al., 2019).

To test the sensitivity of the base DFN structural model, an alternative fracture network model was built from both the localized wellbore image data and regional structural data. Detailed field mapping of veins and breccias to the southeast of the SSGF provide significant data in support of a northwest trending fracture fabric in additional to the north striking fabric within the SSGF for all types of veins (Willis and Tosdal, 1992). Further, the James et al. (1987) study of the nearby Heber geothermal reservoir defines NW striking strike-slip faults and NE trending normal faults with enhanced permeabilities over a broad area. A comprehensive refraction seismic survey across the Imperial Valley delineated these NW trending structural features and revealed evident NE trending features that cut the crystalline basement rocks within the Brawley seismic zone (Fuis et al., 1982). These features are interpreted as NE striking active transfer faults (Fuis et al., 1982; Sims, 2023). The alternative fracture network model of this study combined these NW and NE oriented regional fracture sets with a Poisson distribution of the north striking fractures observed in wellbore image data that yields a significantly higher fracture surface area per unit volume than the base DFN model (Figure 5, all fracture sets).

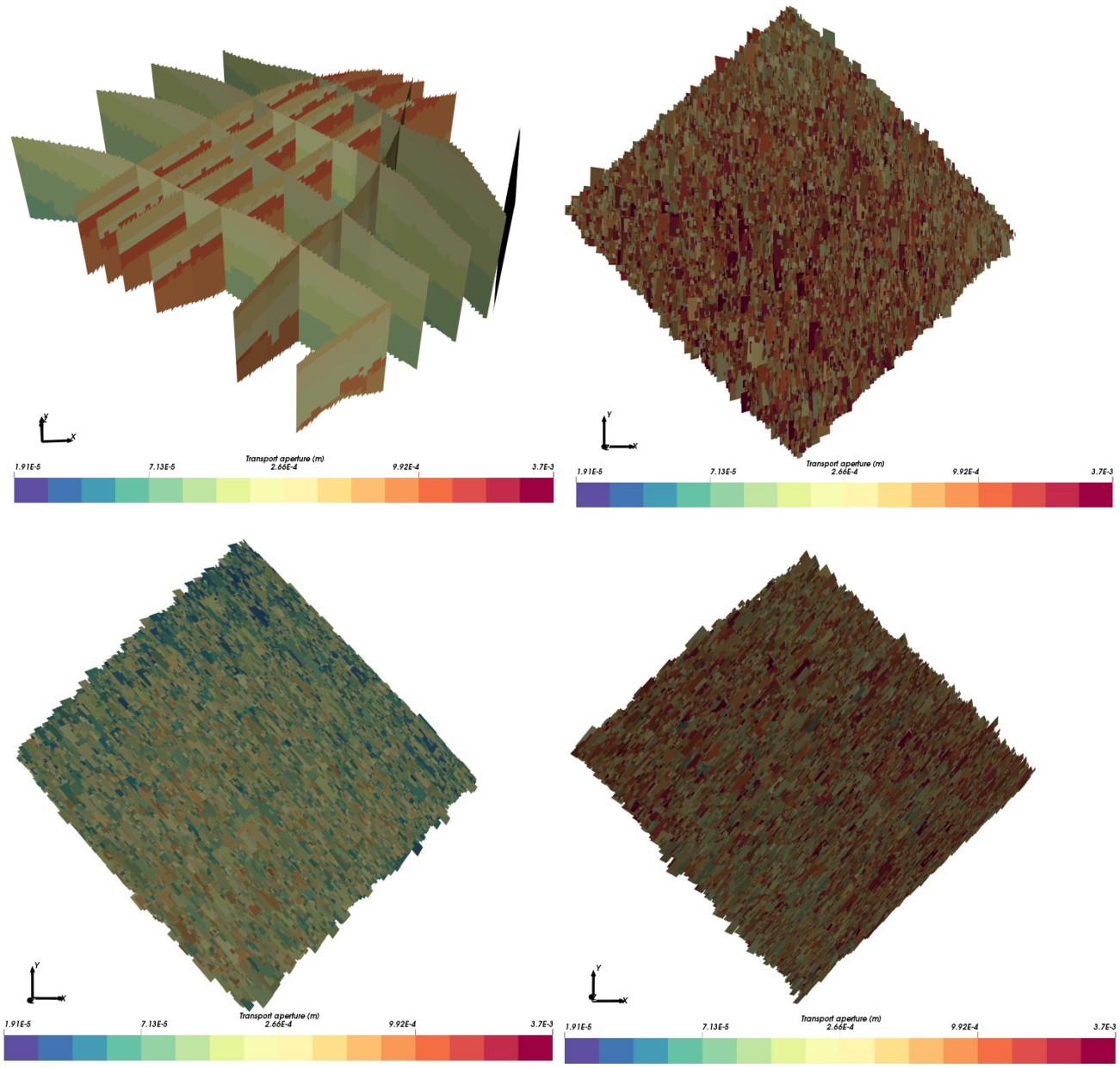

Figure 5. Deterministic faults (top left) and stochastically generated fractures Set 1 (top right) of the base DFN model. Stochastically generated fractures Set 2 bottom left and Set 3 bottom right are added for the alternative fracture network model built on localized wellbore image data and regional structural data.

Stress aperture coupling facilitates the analysis of the sensitivity of the natural fractures and faults to in situ stress that can be used to optimize well design and thereby enhance production. This approach also provides constraints to further refine and calibrate DFN transmissivity calculations.

The stress-aperture coupling within this study uses the compliance model of Moos and Barton (2008). Normal stress is calculated for each fracture plane according to its orientation relative to the maximum horizontal, minimum horizontal, and vertical stress components of the geomechanical model. The effective normal stress (σ_{eff}) to each fracture is then evaluated as:

$$\sigma_{eff} = \sigma_n - P_p$$

Where σ_n is the normal stress at the fracture face and P_p the reservoir pore pressure local to each fracture. Hydraulic aperture is then calculated as:

$$a_h = \frac{A}{1 + 9\frac{\sigma_{eff}}{B}}\hat{a}_h,$$

for an unstressed aperture a_h, aperture factor A, stressed aperture $\hat{a}_h$, and closure stress B that require field specific calibration. A log-normal distribution is assumed for hydraulic aperture with the mean increasing with fracture length (Klimczak et al., 2010). This aperture is then adjusted according to the effective normal stress on the fracture plane based on the stress field and pore pressure provided by the 3D geomechanical model at the center of each fracture using the above formula. In this way, the model captures spatial variability in fracture distribution, inter-connectivity, anisotropy, and hydraulic properties, as constrained by an integrated data analysis. The effect of incorporating stress anisotropy in DFN models is evident in Figure 5 where calculated transport apertures of the deterministic NE- SW oriented faults are higher than those of NW-SE trending faults. Similarly, stochastically generated natural fractures oriented N-S and NE-SW, have higher transport aperture than those oriented NW-SE.

The transmissivities derived from the DFN models were upscaled to a hydraulic conductivity tensor for the reservoir volume (Figure 6). The resultant permeability was calibrated against measured production log data acquired in the two wells within the study area. The resulting upscaled parameters are a directional hydraulic conductivity tensor, fracture kinematic porosity, and other transport properties. A flux-based upscaling method is used that requires several flow calculations through a DFN model calculated for each head gradient direction. The hydraulic conductivity tensor is then derived by a least-squares fit to these flux responses for the fixed head gradients. Figure 6 compares the K_x, K_y, K_z permeabilities of the base DFN model (which range from 6.3E-05mD to 1.3E02mD, top row) with those of the revised DFN model (which range from 3.3E-05mD to 7.5E02mD, bottom row). The interconnected fractures of the revised DFN model have a more uniform and significantly higher permeability distribution than the more conservative base DFN model.

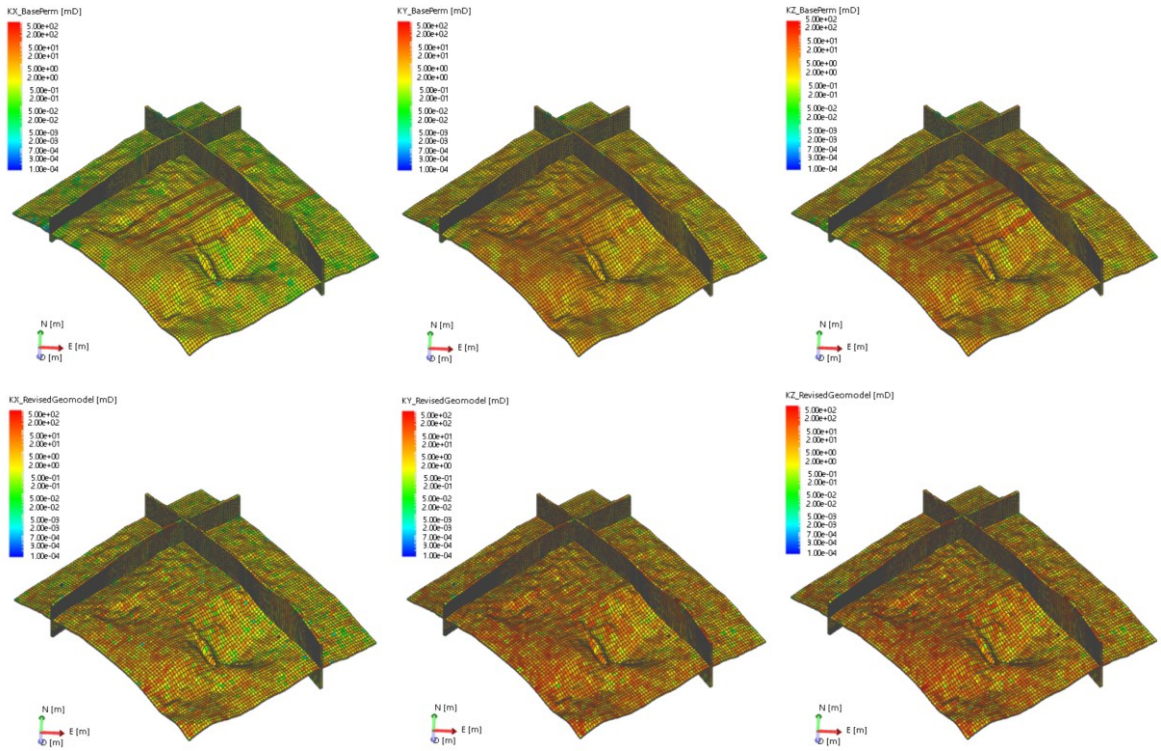

Figure 6: Upscaled base geomodel permeability distribution K_x (left), K_y (center), K_z (right) (top row) and revised geomodel permeability distribution (bottom row).

The variability in permeability laterally and vertically is consistent with the geologic model of convective heat flow up one or more of the large-scale regional faults and their immediate damage zones crosscutting the reservoir. High temperature brines flow from the heat source located below the clinopyroxene zone at the base of the dual porosity reservoir, and to the southwest of the study area, along permeable NE-SW faults.

This methodology is unique in that it can capture the underlying fracture dominated heterogeneity in the permeability field. The hydrostructural DFN modeling approach explicitly incorporates the geometry and properties of discrete features as a central component

controlling flow and transport. The corresponding permeability tensor provides, in an average sense, the effective permeability tensor for each block composed of fractures in dynamic fluid modeling to explore well engineering scenarios for optimal production.

5. RESERVOIR MODELING

5.1 Model Construction

The 3D static base model was imported to the reservoir simulation software. The model consists of 57,000 grid blocks and covers an area of 8 km by 8.6 km with average block dimensions of 200 m by 200 m and an average grid thickness of 110 m (Figure 7). Porosity varies by depth. Permeabilities developed through DFN modeling provide the x, y, z permeability heterogeneity throughout the volume. The initialized thermal properties of the rock and the fluid used in the model are listed in left column of Table 1. The volumetric heat capacity and thermal conductivity of the overburden were then tuned to maintain a constant temperature at the top of the reservoir. The final values are listed in the right column of Table l.

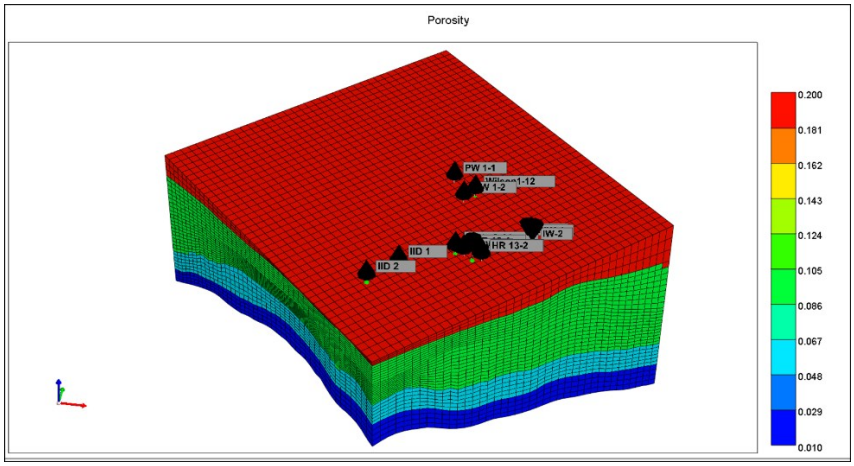

Figure 7. 3D view of the dynamic model displaying the porosity volume.

Table 1 Thermal properties applied to dynamic reservoir modeling

Thermal Property	Initialization Values	Final Values
Volumetric heat capacity rock [J/(m3-°C)]	2.30E+06	2.00E+20
Heat conductivity rock [J/(m*day*°C)]	1.73E+05	2.10E+06
Heat conductivity brine [J/(m*day*°C)]	5.35E+04	—

5.2 Natural State Matching

Heat is distributed in the reservoir by both conduction and convection. The convective heat transfer occurs through fluid circulation due to the almost 100°C temperature difference that exists between the bottom and the top of the reservoir. There is also active upflow, lateral inflow and lateral outflow to the dual porosity reservoir that affects the heat distribution.

The model was initiated with a temperature lower than the reservoir temperature at the natural state and the reservoir parameters, including heat rate at the bottom and the boundary conditions, were tuned to match the measured temperature and pressure data (natural state) after a modelled period of 100 years (at which continued changes in modelled conditions are negligible). Upflow and outflow achieved equilibrium after 100 years and stayed constant at 1550 tonne/hr until the end of the natural state simulation at 10,000 years. Temperature and pressure outputs from the model were compared against available measured profiles from the wells (Figure 8). Key adjustments included fine-tuning permeability, inflow and outflow rates, location of the inflow and outflow zones and fracture density parameters. Iterative runs were performed until the model outputs aligned closely with the observed data. Figure 9 shows the temperature comparison between the static model (orange curve), well logs (red curve), base case geomodel (blue curve) and sensitivity cases described in the following sections.

The model's pressure distribution at the natural state condition matched the measured pressure data. This indicates that the brine density versus pressure as a function of salinity was correctly modelled. Additionally, the correct pressure distribution was established in the presence of the active upflow and outflow. The successful natural state matching provided a robust baseline model that accurately

represented the reservoir's undisturbed conditions. This ensured greater confidence in subsequent dynamic simulations of production and injection scenarios, enabling more reliable forecasts and optimization strategies.

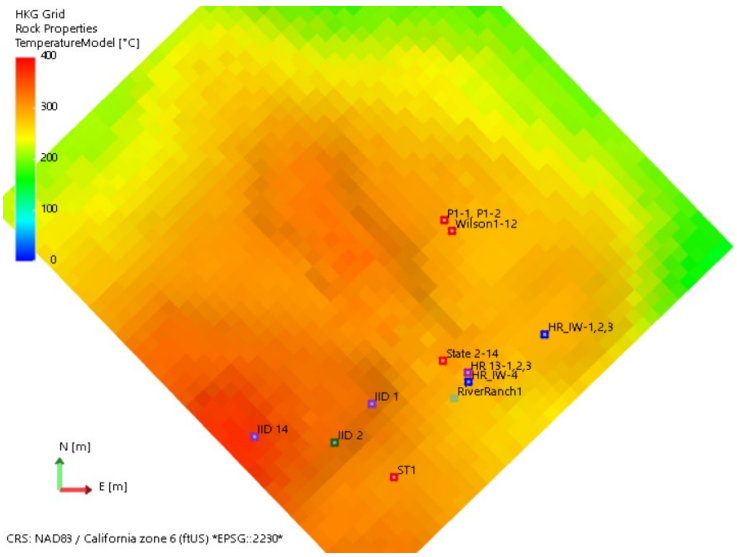

Figure 8: Location of wells used for natural state model validation.

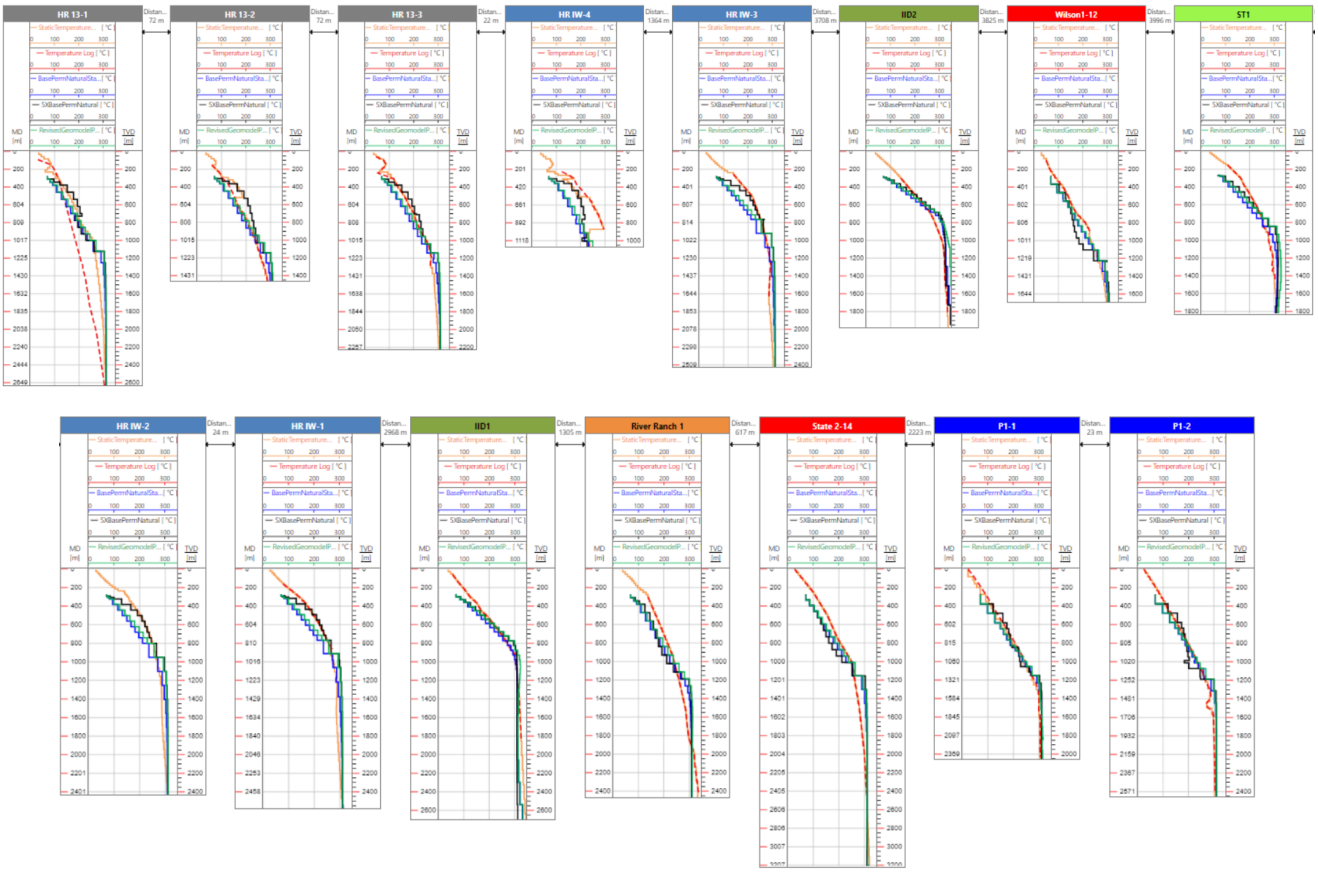

---- Static Temperature Model - - - Well Log Temperature ---- Base DFN Model
---- Enhanced Permeability Model ---- Revised DFN Model

Figure 9: Temperature versus depth comparison for the natural state models.

5.3 Initial Stage Production and Injection

The Initial Stage concept included 3 production wells and 4 injection wells that were open at the start of the forecast. Production wells were controlled by the maximum brine production rate of 246 kg/s and the minimum wellhead pressure of 1930 kPa. It was assumed that 95% of the produced brine was injected back into the reservoir.

Injection rates were assigned to the four injection wells on Pad A and their directionally drilled trajectories were optimized to reduce the risk of thermal and chemical breakthrough. The injection wells were controlled by a maximum wellhead pressure of 4137 kPa and maximum brine injection rate. The injection temperature was set to 60°C, and the lithium concentration was 7 ppm, consistent with the Initial Stage facility design.

Production wells maintained a constant brine production rate of 2662 tonne/hr during the forecast and no decline was observed (Figure 10).

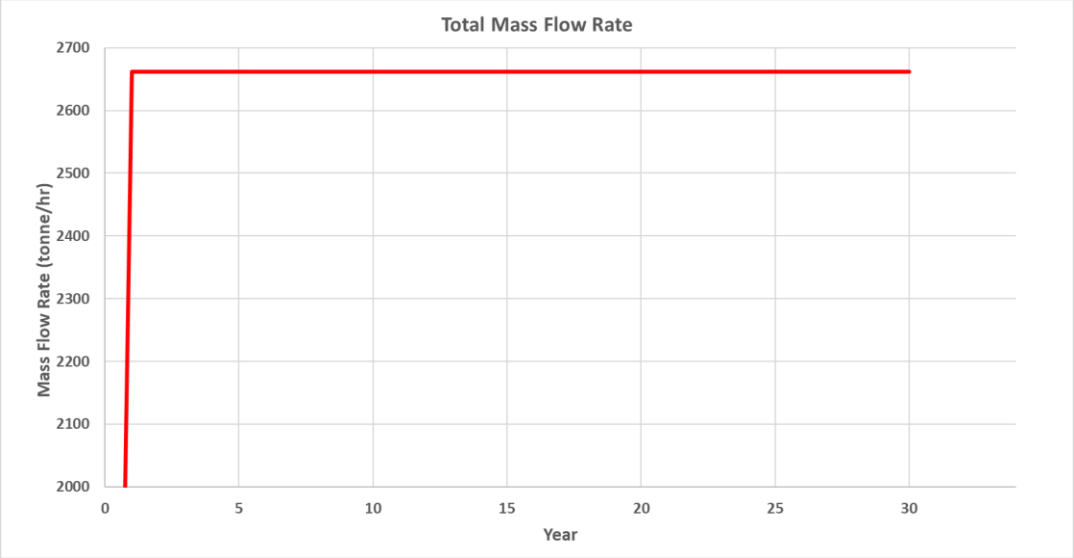

Figure 10: Total mass flow rate for the Initial Stage.

The reservoir single-phase enthalpy of production fluids prior to heat loss in boiling varied slightly in each well due to the differences in the bottom-hole temperature but stayed relatively constant during the forecast for each well (Figure 11). The total energy rate reached 7.4×10^{13} J/day, equivalent to an enthalpy production rate of 463 BTU/lbm or 1076 kJ/kg.

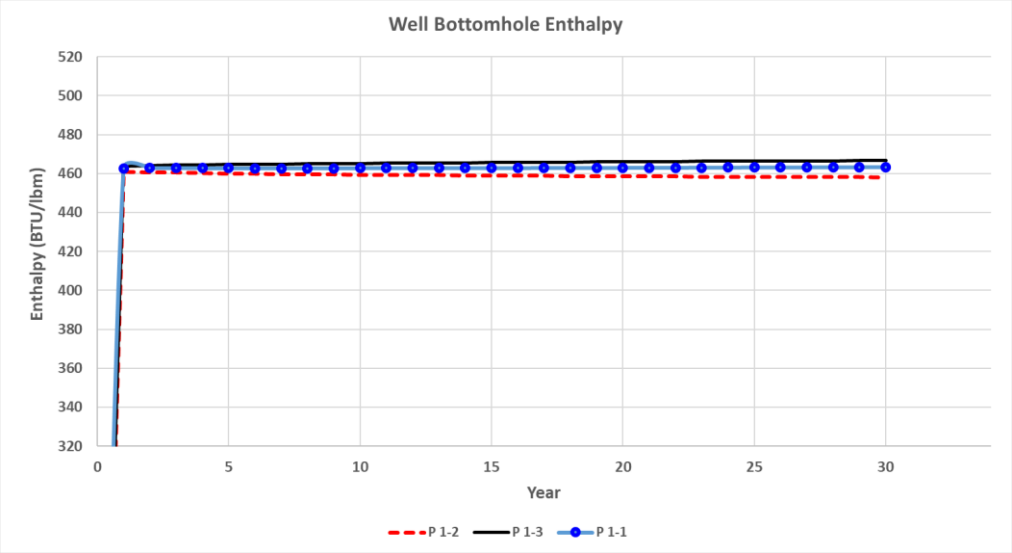

Figure 11: Production well single-phase reservoir enthalpies for the Initial Stage.

The modelled elemental lithium concentration showed a 4.6% decline in Well P1-1. It was constant in the production fluid of Well P1-2 and declined by 1% in Well P1-3 after 30 years. This decline in lithium concentration is attributed to chemical breakthrough (as opposed to thermal breakthrough) from the injection wells to production wells, a common occurrence in some reservoirs due to a pressure sink around the production wells and communication through connected fracture networks. Well P1-1 is extended in the direction of the injection well locations, and it showed the highest decline in lithium concentration. The total elemental lithium production rate (and concentration) for the Initial Stage declined by 1.9% over 30 years and dropped from 0.613 tonne/hr to 0.602 tonne/hr (Figure 12).

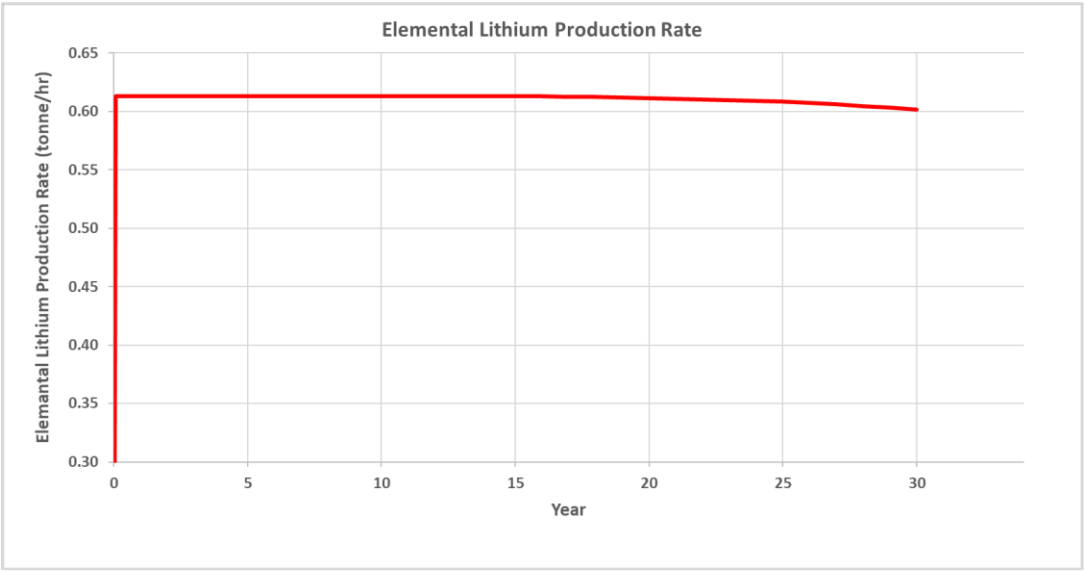

Figure 12: Elemental lithium production rate for the Initial Stage.

Cumulative elemental lithium production modelled from the three production wells in the Initial Stage increases linearly and reaches 160,000 tonnes over the 30 years (Figure 13).

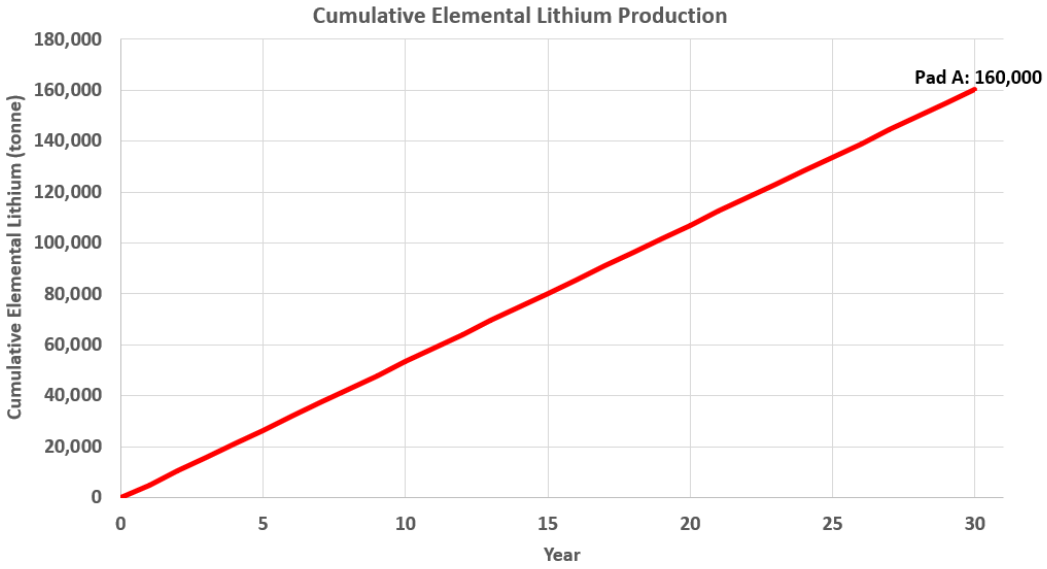

Figure 13: Cumulative elemental lithium production over 30 years for the Initial Stage.

5.4 Sensitivity Assessment

Sensitivity to Injection Well Location

Three injection pads (Pad A, Pad B, and Pad C) were tested for the Initial Stage. The same operating controls described above were applied to injection wells on Pads B and C. The injection pads are located approximately 2900 m (Pad A), 1300 m (Pad B), and 800 m (Pad C) from the producers. Figure 14 presents the results of the three scenarios. Pad B forecasts 20% less, and Pad C forecasts 11% less lithium production than the Pad A scenario. The Pad A location is recommended for production in the Initial Stage.

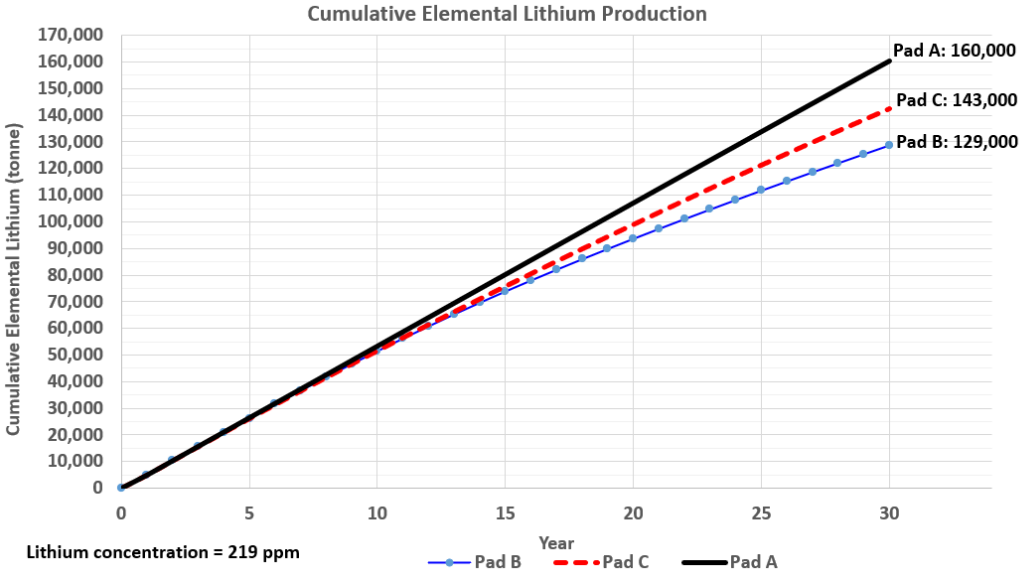

Figure 14: Cumulative elemental lithium production sensitivity to injection well location.

Sensitivity to Permeability Magnitude

An Enhanced Permeability case was evaluated to test the effect of increased permeability relative to the Base Case described above. For this analysis, a five-fold increase in fieldwide reservoir permeability was used to forecast production for Pad A in the Initial Stage concept.

This five-fold permeability factor was based on additional analysis of the P1-2 well test, which suggested the base permeability was conservative. The permeability increase was applied across the entire model volume. The natural state was again modeled using the same boundary conditions as the base model to evaluate the impact of an increase in permeability. The Enhanced Permeability natural state model presented in Figure 9 (black curve) shows this global increase in permeability remains a very good match to field data of temperatures across the site. In many cases, the match is a better fit than was the base case permeability model (c.f., IW-1, IW-2, IW-3, HR-13-1, HR-13-2, HR-13-3).

As with the Base Case, single-phase reservoir enthalpy varied slightly due to the differences in the bottom-hole temperature but stayed constant at 463 BTU/lbm throughout the forecast, which shows that injected fluid is completely reheated along the flow path. The lithium production rate for the Enhanced Permeability case declined by 0.9% from 0.613 tonne/hr to 0.608 tonne/hr over 30 years. This decline is improved from the 1.9% decline modelled for the Base Case (Figure 15). The Enhanced Permeability cumulative elemental lithium production from the three production wells was about 1% higher than for the Base Case and reached 161,000 tonnes (Figure 16).

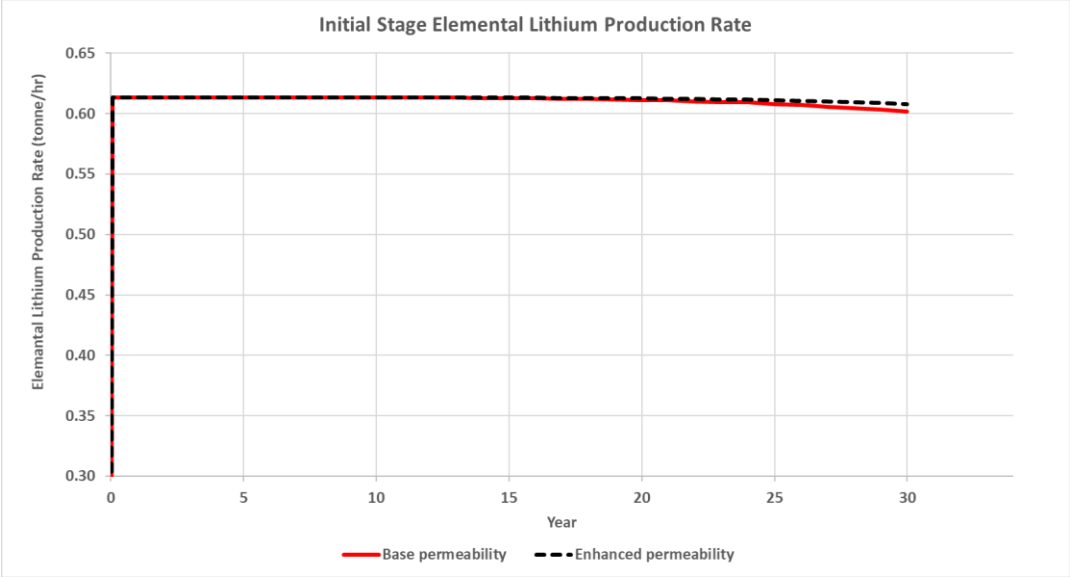

Figure 15: Elemental lithium production rate sensitivity to permeability variations.

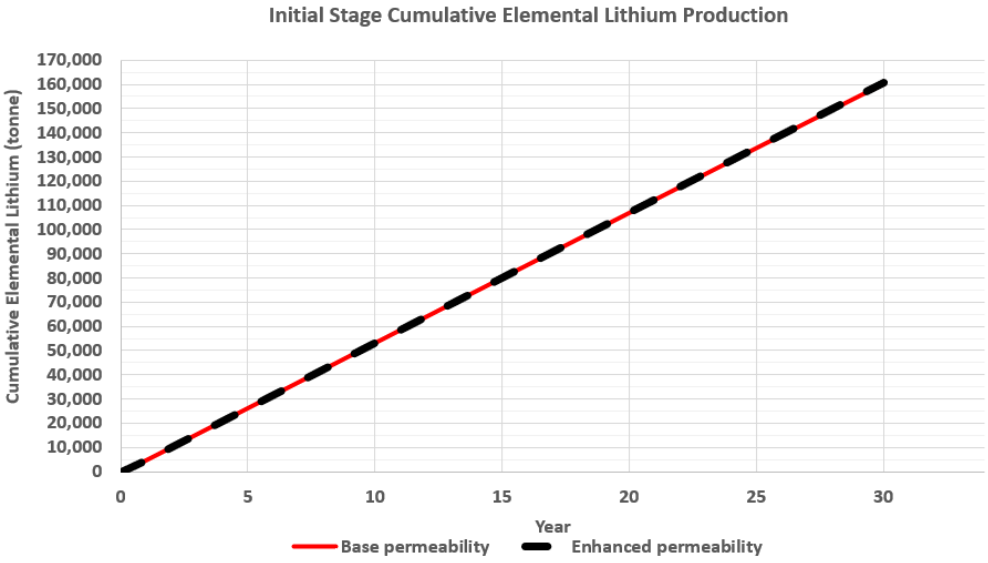

Figure 16: Cumulative elemental lithium production sensitivity to permeability variations.

Sensitivity to Permeability Distribution.

A Revised Permeability distribution case was evaluated to test the impact of variability in natural fracture distribution relative to the Base Case as described above. For this analysis, the Revised DFN geomodel was used to define the permeability heterogeneity across the field. The natural state was again modeled using the same boundary conditions as the base model to evaluate the impact of variation in permeability distribution. This scenario was used to compare the cumulative elemental lithium production for Pads B and C relative to Pad A in the Initial Stage concept.

The cumulative lithium production for the Pad B case location remained relatively unchanged and shows the lowest results, however, the Pad C case is significantly improved compared to the base permeability distribution (Figure 17). The Pad C forecast is only 2% less cumulative lithium production than that of Pad A. Using the base permeability model, the Pad C forecast was 11% less than the Pad A case.

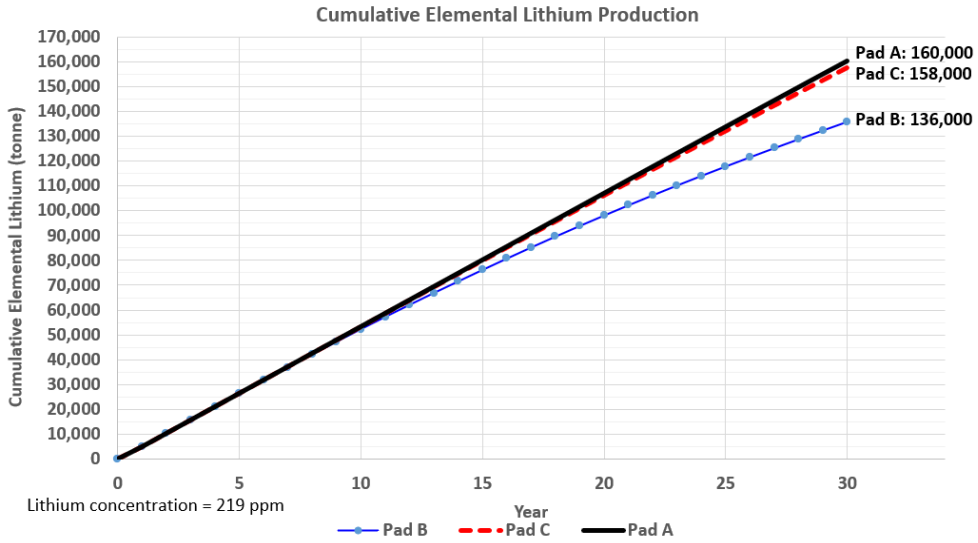

Figure 17: Cumulative elemental lithium production sensitivity to permeability distribution.

6. CONCLUSIONS

This study has integrated available subsurface data to provide a realistic, possible base-case description of the targeted geothermal resource. Focus was placed on updating the thermal model through a zone-based alteration minerology model described by HKG (Sims and Neuhoff, 2018) tied to present day recorded temperatures.

The productivity-hosting fracture system present within the reservoir was modelled using a discrete fracture network (DFN), with input derived from wellbore image data and the fault framework. 1D to 3D geomechanical modeling provided input to dynamically computed stress-permeability coupling during DFN model development. A halocline "zone" at a temperature of approximately 260°C is well defined in the literature and is included in the model. The halocline has a significant effect on reservoir fluid densities in the dynamic model. The change in density provides a barrier to upward convective flow of sub-halocline fluids, which cannot pass through a less dense liquid.

The static model was imported into a commercial reservoir modelling package for dynamic simulation. The model's pressure distribution at the natural state condition matched measured pressure and salinity data and provided an excellent match to a large spatial distribution of well temperature data. Forecast scenarios, designed to evaluate optimal initial stage production, were simulated for a 30-year forecast of enthalpy and lithium production. In all scenarios, the well field was optimized in terms of well geometry and spacing within the permeability distribution and alignment of reservoir flow. In the best-case Stage 1 Plan A scenario, production wells maintained a constant fluid brine production rate during the forecast and little decline was observed. The reservoir single-phase enthalpy of production fluids prior to wellbore heat loss varied slightly due to the differences in the bottom-hole temperature but stayed constant during the forecast for each well. The total elemental lithium production rate (and concentration) for Stage 1 Plan A base model declined by 1.9% over 30 years and dropped from 0.613 tonne/hr to 0.602 tonne/hr. Cumulative elemental lithium production modelled from the three producers of Scenario Stage 1 Plan A (injection from the furthest location modelled for Stage 1) reaches 160,000 tonnes over 30 years. Sensitivities to production forecasts were tested for permeability magnitude, well location, and permeability distribution. These sensitivity analyses illuminate the additional data and analyses required to reduce uncertainties in reservoir model forecasting.

Key observations of this study are: 1) accurate representation of the thermal and chemical stratification of the halocline density gradient is crucial for limiting vertical mixing; 2) calibrated DFN modeling is essential for optimizing well placement and achieving sustainable production in the fracture-driven flow system of the SSGF; 3) proper injection strategies reduce the risk of thermal short-circuiting and

chemical degradation of the reservoir; and 4) operational trade-offs underscored by sensitivity analyses show the need for a balanced approach to well spacing, permeability management, and production optimization.

The use of state-of-the-art geological and reservoir modeling techniques derived from the oil and gas industry has provided a robust analysis of the production performance and a framework for wellfield development. An exhaustive natural state matching process has achieved a robust model fit with observed data to give a high level of confidence in the three-dimensional porosity and permeability field. This fit is achieved only by using a deep circulation assumption, proposed and supported by extensive work of HKG, where fluids flow upward from below the reservoir and a three-dimensional DFN provides highly permeable fracture flow, both of which are consistent with geothermal industry experience in the SSGF. The development of the model derived for this study and discussed in this paper is ongoing to accommodate extending its depth and lateral extent and to implement modifications to the governing Equation of State that are appropriate for deeper higher-temperature magmatic hydrothermal processes. Data informing this model will be expanded to capture the comprehensive geologic framework of Sims et al (2025).

The HKG project represents a significant opportunity for harnessing geothermal energy and extracting critical minerals such as lithium. This study developed and validated a dynamic reservoir model that integrates geological, geomechanical, and geochemical data to provide actionable insights into resource development.

ACKNOWLEDGEMENT

We thank the management of Hell's Kitchen Geothermal LLC for their support of the work and permission to present this paper.

REFERENCES

Araya, N. and John O'Sullivan, J.: A 3D Conceptual and Natural-State Model of the Salton Sea Geothermal Field, GRC transactions 46, (2022), 2123-2159.

Dershowitz, W., LaPointe, P.R., Doe, T.: Advances in Discrete Fracture Network Modeling. Proceedings of the US EPA/NGWA fractured rock conference, Portland, (2004), 882-894.

Dobson, P. et al.: Characterizing the Geothermal Lithium Resource at Salton Sea, Lawrence Berkeley National Laboratory Energy Geosciences, LBNL-2001557, (2023). https://escholarship.org/uc/item/4x8868mf.

Dutcher, L.C., Hardt, W.F., and Moyle, W.R.: Preliminary Appraisal of Ground Water in Storage with Reference to Geothermal Resources in the Imperial Valley Area, California. Geological Survey Circular (1972), 649.

Fuis, G.S., Mooney, W.D., Healey, J.H., McMechan, G.A.: Crustal Structure of the Imperial Valley Region; *in* The Imperial Valley, California, Earthquake of October 15, 1979. Geological Survey Professional Paper 1254, (1982), 25–49, https://pubs.usgs.gov/publication/pp1254.

Helgeson, H.C.: Geologic and thermodynamic characteristics of the Salton Sea geothermal system. Amer. J. Sci. 266: No.3, (1968), 129–166.

James, E. D., Hoang, V.T., Epperson, I. J.: Structure, Permeability and Production Characteristics of the Heber, California Geothermal Field. PROCEEDINGS, Twelfth Workshop on Geothermal Reservoir Engineering, Stanford University, Stanford, California, SGP-TR- 109, January 20-22, (1987).

Jia, R., Liu, B., Fu, X., Gong, L., and Liu. Z.: Transformation Mechanism of a Fault and Its Associated Microstructures in Low-Porosity Rocks: A Case Study of the Tanan Depression in the Hailar-Tamtsag Basin. Journal of Marine Science Engineering 7, 286; (2019), 1-17. https://doi.org/10.3390/jmse7090286.

Klimczak, C., Schultz, R.A., Parashar, R. and Reeves, D.M.: Cubic law with aperture-length correlation: implications for network scale fluid flow. Hydrogeology Journal, 18, (2010), 851-862, DOI 10.1007/s10040-009-0572-6.

Moos, D. Barton, C. A.: Modeling uncertainty in the permeability of stress-sensitive fractures. ARMA, Paper #:08-312, (2008).

Moore, J. N. and Adams, M.C.: Evolution of the Thermal Cap in Two Wells from the Salton Sea Geothermal System, California, Proceedings, Thirteenth Workshop on Geothermal Reservoir Engineering, Stanford University, Stanford, California, January 19-21, 1988, SGP-TR-113.

Sims, D. B. and Neuhoff, P. S.: Resource Estimation for Hell's Kitchen Lithium Brine Project, Imperial Valley, California, USA, proprietary, (2018).

Sims, D.B.: Analysis for relative locations of Stage 1 injection and production areas, HKG internal report, proprietary, (2022), 61p.

Sims, D.B.: SSGF Regional Structure Origin and Characteristics, Controlled Thermal Resources, Confidential Internal Report, (2023).

Sims, D. B.: Neuhoff, P. S., and Norton, D.L., Structural, Mineralogical, and Geophysical Data Implications for the Development of the Salton Sea Magmatic Hydrothermal System, Proceedings, 50th Workshop on Geothermal Reservoir Engineering Stanford University, Stanford, California. SGP-TR-229, (2025).

Thompson, A. Demir, Z. Moran, J., Mason, D., Wagoner, J., Kollet, S., Mansoor, K., McKereghan, P.: Groundwater availability Within the Salton Sea Basin, Final Report, Lawrence Livermore National Laboratory, LLNL-TR-400426, (2008).

Willis, G.F., Tosdal, R.M.: Formation of Gold Veins and Breccias during Dextral Strike-Slip Faulting in the Mesquite Mining District, Southeastern California. Economic Geology, 87, (1992), 2002-2022. http://pubs.geoscienceworld.org/books/book/chapter-pdf/3808703/9781629490304_backmatter.pdf.

Williams, A.E., and McKibben, M.A.: A brine interface in the Salton Sea Geothermal System, California: Fluid geochemical and isotopic characteristics. Geochimica et Cosmochimica Acta, 53, (1989), 1905-1920. https://doi.org/10.1016/0016-7037(89)90312-8.

Williams, A.E.: Fluid density distribution in a high temperature, stratified thermohaline system: implications for saline hydrothermal circulation. Earth and Planetary Science Letters, 146, (1997), 121-136.